Petroleum Science 23 (2026) 2106–2119

Contents lists available at ScienceDirect

Petroleum Science

journal homepage: www.keaipublishing.com/en/journals/petroleum-science

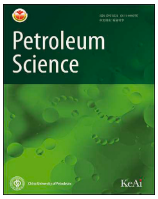

Original Paper

Chloride-dependent enhancement of microbiologically influenced corrosion on X80 steel by *Desulfovibrio desulfuricans*: The critical role of extracellular polymeric substances

Jia-Hang Li [a,b], En-Ze Zhou [a,b,c,*], Zhong Li [a], Di Wang [a], Fu-Hui Wang [a], Da-Ke Xu [a,**]

[a] *State Key Laboratory of Digital Steel, School of Materials Science and Engineering, Northeastern University, Shenyang, 110819, Liaoning, China*
[b] *National Key Laboratory of Marine Corrosion and Protection, Luoyang Ship Material Research Institute, Luoyang, 471023, Henan, China*
[c] *Foshan Graduate School of Innovation, Northeastern University, Foshan, 528311, Guangdong, China*

ARTICLE INFO

Article history:
Received 14 July 2025
Received in revised form
22 September 2025
Accepted 2 December 2025
Available online 8 December 2025

Edited by Teng Zhu

Keywords:
Steel
Chloride
Sulfate-reducing bacteria
Microbiologically influenced corrosion
Extracellular polymeric substances
Extracellular electron transfer

ABSTRACT

Microbiologically influenced corrosion (MIC) and chloride ion attack represent principal factors contributing to the premature failure of marine metallic infrastructures. This study systematically investigated the MIC behavior of X80 steel induced by sulfate-reducing bacteria (SRB) in simulated marine environments with varying chloride concentrations. Under sterile anaerobic conditions, elevated chloride concentrations slightly accelerated the corrosion of X80 steel. However, the biotic system (30 g/L Cl^-) exhibited an order-of-magnitude increase in the corrosion rate of X80 steel compared to sterile controls. The relative corrosion severity in SRB-inoculated environments followed the descending order: 30 g/L > 10 g/L > 20 g/L > 5 g/L Cl^-. Chloride concentration critically modulated SRB metabolic activity. Sulfate reduction rates at 5 g/L Cl^- demonstrated a significant 85% reduction relative to optimal conditions at 20 g/L Cl^-, correlating with near-complete bacterial growth inhibition. Intriguingly, suboptimal chloride environments (10 and 30 g/L Cl^-) triggered substantial extracellular polymeric substance (EPS) production, serving as a protective barrier and ionic exchange medium. EPS exacerbated steel corrosion by accelerating anodic dissolution through complexation with ferrous ions. Fourier-transform infrared spectroscopy results confirmed that EPS contains redox-active functional groups. Injecting 1 g/L EPS into SRB broth increased the corrosion current density from 9.2 ± 0.8 μA/cm^2 to 14.3 ± 1.2 μA/cm^2. These findings provide new insights into the dual role of EPS in MIC processes, emphasizing its critical function in extracellular electron transfer-MIC mechanisms.

1. Introduction

The development of offshore oil and gas resources is inseparable from marine engineering equipment, and the operational demands in extreme environments impose rigorous requirements on material performance. High-strength steel is widely used in various marine applications, such as oil and gas pipelines and drilling platforms, due to its superior mechanical properties and cost efficiency. However, corrosion is a primary limiting factor for its safe application in marine environments (Dong et al., 2023; Niu et al., 2024). The severity of marine corrosion stems from the high salinity, particularly the chloride content in seawater and microbial colonization. Marine microbiologically influenced corrosion (MIC), characterized by its unpredictability and complexity, critically endangered the integrity of marine welded structural infrastructure, amplifying both economic losses and safety risks (Xie et al., 2023; Wang et al., 2024a; Li et al., 2025a). Global statistics indicate that MIC causes annual economic losses amounting to US$2.7 trillion (Xu et al., 2023), with MIC-related failures accounting for 20% of total economic losses attributed to marine corrosion (Little et al., 2020; Tuck et al., 2022). This economic imperative underscores the urgency to decipher MIC mechanisms in marine environments.

---

* Corresponding author.
** Corresponding author.
E-mail addresses: zhouenze@smm.neu.edu.cn (E.-Z. Zhou), xudake@mail.neu.edu.cn (D.-K. Xu).

Peer review under the responsibility of China University of Petroleum (Beijing).

https://doi.org/10.1016/j.petsci.2025.12.004
1995-8226/

In marine microbial ecosystems, sulfate-reducing bacteria (SRB) have been widely acknowledged as the predominant etiological agents of MIC, accounting for over 50% of total MIC-related economic losses in marine infrastructure (Zhang and Wu, 2020). Under sustained carbon-limited conditions characteristic of marine environments, SRB demonstrate remarkable corrosion aggressiveness, inducing extensive and severe pitting corrosion on carbon steel substrates (Liu et al., 2022a). This corrosive capacity stems from dual mechanisms: 1) secretion of acidic metabolic byproducts causing metabolites-MIC, and 2) electron uptake capability from metal surfaces via extracellular electron transfer (EET) (Ueki and Lovley, 2022). Crucially, both corrosion mechanisms fundamentally depend on microbial metabolic dynamics regulated by environmental conditions. Therefore, to advance mechanistic understanding of MIC phenomena under ecologically relevant marine conditions, systematic investigation of environmental modulators on microbial metabolic activity and their subsequent corrosion implications is imperative.

Chloride ions constitute approximately half of the ionic composition in marine environments, representing a defining parameter of marine environments. However, chloride ion concentrations exhibit significant spatiotemporal variations governed by thermal gradients, ocean current dynamics, and tidal fluctuations, which exert profound impacts on microbial metabolic activities and thus affect MIC. The chloride-mediated MIC acceleration in marine environments has been documented. It has been reported that chlorides can accelerate MIC of titanium alloys induced by *Shewanella algae*, which is related to the disruption of the passive film by chloride ions (Li et al., 2021). Additionally, chloride ions can enhance MIC associated with SRB (Xie et al., 2019; Wang et al., 2024b), but the metabolic interplay between chloride ion and MIC remains poorly understood. This knowledge gap highlights the imperative to elucidate the interactions between chloride ions and microbial metabolism to gain a comprehensive understanding of MIC mechanisms of materials in marine environments.

A suboptimal chloride environment inhibits the growth and metabolic activity of the microbial population (Bharti et al., 2015). To cope with this environment, microorganisms develop various adaptive strategies, including osmolyte accumulation, membrane lipid modification (Forni et al., 2017; Meneses et al., 2017; Morra et al., 2018), and extracellular polymeric substance (EPS) secretion for biofilm formation (Liu et al., 2022b; Chakraborty and Mondal, 2023). EPS matrices demonstrate multifunctional roles: providing cellular nutrition through their protective layers (Isfahani et al., 2018), forming structurally ordered corrosion barriers via unique rheological properties (Gao et al., 2024), and generating biomineralized coatings through marine inorganic interactions (Li et al., 2019; Gao et al., 2022; Hao et al., 2022). Paradoxically, while EPS may retard general corrosion through diffusion barrier effects, electroactive bacteria may utilize EPS to facilitate MIC through redox-active components that mediate electron transfer (He et al., 2022; Liu et al., 2022c; Fu et al., 2023). For instance, EPS produced by *Shewanella oneidensis* MR-1 has been demonstrated to mediate long-range electron transfer (Xiao et al., 2017). Such dual functionality highlights the critical need for a systematic investigation into the role of SRB-derived EPS under a suboptimal chloride environment.

This study investigated the effect of chloride ions on MIC induced by *Desulfovibrio desulfuricans* (*D. desulfuricans*) through biofilm characterization, polysaccharide-protein staining, electrochemical measurements, pitting assessment, and corrosion product analysis. We further examined the impact of chloride ions on the secretion of EPS by *D. desulfuricans* and explored EPS-Fe^{2+} complexation using ultraviolet–visible (UV–Vis) spectroscopy and Fourier-transform infrared (FT-IR) spectroscopy. By analyzing electrochemical responses, we also evaluated the role of EPS as an electron shuttle in EET-MIC of X80 pipeline steel caused by *D. desulfuricans*. Our findings culminated in a proposed mechanistic framework for MIC induced by SRB under suboptimal chloride environments. Understanding these mechanisms could inform effective MIC mitigation strategies in marine settings.

2. Experimental

2.1. Materials and bacterial cultivation

The X80 steel with a composition (wt%) of: C 0.049, Si 0.18, Mn 1.83, S 0.0002, P 0.012, Mo 0.08, Ni 0.24, V 0.0001, Cr 0.026, N 0.01, Cu 0.14, and Fe balance, was used in this work. The X80 steel was cut into square coupons measuring 10 mm × 10 mm × 3 mm. The coupons were sequentially abraded to a 1000-grit finish, followed by ultrasonic cleaning in deionized water and anhydrous ethanol for 10 min, and then air dried.

The bacterial strain used in this work was *D. desulfuricans* (ATCC 27774). The artificial seawater contained (g/L): NaCl 24.35, $MgCl_2$ 5.2, Na_2SO_4 4.09, $CaCl_2$ 1.16, KCl 0.695, $NaHCO_3$ 0.201, KBr 0.101, and K_2HPO_4 0.05. The microbial culture medium was formulated by enriched artificial seawater (EASW) with 28.3 mM sulfate serving as the electron acceptor and supplemented with 60 mM Na-DL-lactate as the electron donor. Additionally, 1 mL of trace element solution SL-10 and 10 mL of Wolin's vitamin solution (detailed composition provided in Supplementary Note 1) were added. The Wolin's vitamin solution was sterilized using a 0.22-μm sterile filter (Millex-GP, MilliporeSigma, USA), while all other components were autoclaved at 121 °C for 20 min. To ensure an anaerobic environment (O_2 content <0.1 ppm), the medium was continuously purged with high-purity N_2 (99.99%) before use. All SRB inoculations were conducted inside an anaerobic incubator. The medium pH was adjusted to 8.2 ± 0.1, monitored using an acidimeter (SevenExcellence S400-Basic, Mettler Toledo, Switzerland). The total chloride ion concentration in the medium was 19.71 g/L. *D. desulfuricans* was initially pre-cultured in standard EASW at 30 °C for 3 days and then transferred to fresh EASW media with chloride ion concentrations of 5, 10, 20, and 30 g/L, adjusted by modifying NaCl content. During the experiments, the temperature was maintained at 30 °C using a water bath to ensure cell viability. Media with 5, 10, and 30 g/L chloride ion were defined as suboptimal chloride medium. The Cell growth was monitored using a UV–visible spectrophotometer (Genesys 50, Thermo Fisher Scientific, USA). The sulfate concentration in the medium was analyzed with ion chromatography (Dionex AS-DV, Thermo Scientific, USA).

2.2. Biofilm characterization

For biofilm characterization and corrosion analysis, each 125-mL anaerobic vial contained three X80 steel coupons, 100 mL of EASW medium, and 1 mL of bacterial inoculum. The vials were incubated at 30 °C for 7 days. After incubation, sessile and planktonic cells were counted using a hemocytometer under a 400 × microscope (XSP-2CA, shanghai Optical Instrument Factory, China). Sessile cells were first removed from coupons surface with a sterile cell scraper and resuspended in sterile phosphate-buffered saline (PBS, 0.1 M, pH = 7.4) for counting.

Biofilm morphology was observed using scanning electron microscope (SEM) (EVO 10, Zeiss, Germany) and confocal laser scanning microscope (CLSM) (LSM 900, Zeiss, Germany). For SEM, coupons were rinsed with sterile PBS and biofilms were fixed with 4% (w/w) glutaraldehyde for 4 h. Coupons were dehydrated through a graded ethanol series (60%, 70%, 80%, 90%, 95% and 100% (v/v)), then sputtered with gold to enhance conductivity. For CLSM, the LIVE/DEAD™ BacLight™ Bacterial Viability Kit (Invitrogen, USA) was used to stain live/dead cells. Live cells emitted green fluorescence when stained with SYTO 9, whereas dead cells exhibited red fluorescence upon staining with propidium iodide (PI). The concentrations of the staining solutions were all 10 μL/mL. The staining process was performed in a dark environment at room temperature for 15 min. For analysis of EPS components, biofilm-bearing coupons were first rinsed with sterile PBS and subsequently subjected to sequential staining protocols. The biofilms were permeabilized by immersion in 1% (v/v) Triton X-100 solution for 5 min, followed by staining: Alexa Fluor™ 633 NHS ester (N-hydroxysuccinimidyl ester, Thermo Fisher Scientific, USA) was used for polysaccharide detection over 15 min, and SYPRO™ Tangerine fluorescent dye (Thermo Fisher Scientific, USA) was employed for 15 min protein staining. The concentrations of the staining solutions were all 10 μL/mL. After each staining, rinse gently with sterile PBS. Each staining step performed sequentially under controlled light conditions.

2.3. Weight loss and pitting morphology analysis

Prior to the immersion experiment, the polished coupons were weighed using an analytical balance (ME104E, Mettler Toledo, Switzerland). After 7-d immersion, the coupons were retrieved. According to the sample cleaning standard (ASTM Standard, ASTM G1–25), Clarke's solution was used to remove biofilms and corrosion products. Coupons were ultrasonically cleaned in anhydrous ethanol for 5 min and dried using N_2 (99.99%). Ten coupons were randomly selected from five experimental replicates for weighing. Pit morphology and depth were analyzed using CLSM. Pit density and probability were determined by random analysis of thirty regions across five coupons. Detailed pit probability calculations are provided in Supplementary Note 2. During the experimental period, the pH of the SRB broth was monitored using the acidimeter.

2.4. Corrosion products analysis

After 7-d immersion, coupons were rinsed with sterile PBS to remove planktonic cells. Corrosion products was analyzed using X-ray photoelectron spectroscopy (XPS, ESCALAB 250, Thermo Scientific, USA). High-resolution spectra were calibrated against the C 1s 284.6 eV and processed using with XPS-Peak 4.1 software.

2.5. Electrochemical measurements

Electrochemical tests were performed using a three-electrode cell setup connected to an electrochemical workstation (Reference 600+, Gamry Instruments, USA). The system consisted of a platinum electrode as the auxiliary electrode, a saturated calomel electrode (SCE) as the reference electrode, and X80 steel coupons as the working electrode. Linear polarization resistance (LPR) and electrochemical impedance spectroscopy (EIS) measurements were performed when the open circuit potential (OCP) was steady. The potential of LPR measurement was swept from −10 mV to +10 mV (vs. E_{OCP}) with a scan rate of 0.125 mV/s. EIS measurements were recorded over a frequency range of 10^5 Hz to 10^{-2} Hz with a sinusoid amplitude of 5 mV. For potentiodynamic polarization curve tests, the applied potential was scanned from −0.3 V to +0.3 V (vs. E_{OCP}) at a scan rate of 0.167 mV/s.

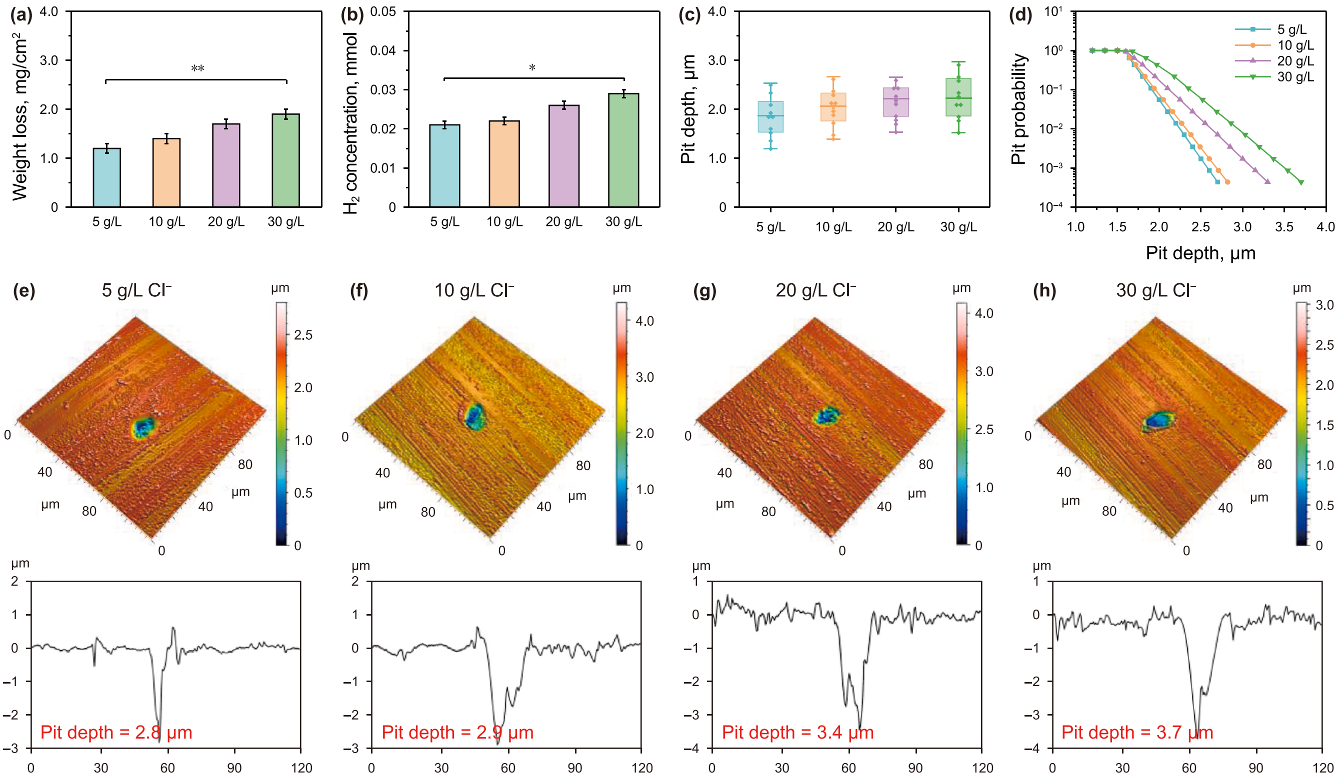

Fig. 1. The effect of chloride concentrations on corrosion of X80 steel in anaerobic sterile EASW medium after 7-d incubation. **(a)** Weight loss, **(b)** headspace hydrogen contents, **(c)** the box chart of pit depths (The box chart is composed of five lines, from top to bottom, which are the maximum value, third quartile, median, quarter quantile and minimum value of the coupon index. The dots are the mean value, **(d)** pit probability, **(e)**–**(h)** the maximum pit morphology. *$P < 0.05$, **$P < 0.01$.

2.6. EPS extraction and characterization

EPS was extracted following established protocols (Li et al., 2021; Gao et al., 2022). Specifically, the medium was centrifuged at 10,000 rpm and 4 °C for 20 min in a high-speed freezer centrifuge (5425R, Eppendorf, Germany) after 7-d cultivation. The supernatant was filtered twice through a 0.22-μm sterile filter to remove residual cells. The filtrate was mixed with two-fold volumes of methanol and stored at 4 °C overnight. The mixture was centrifuged again at 10,000 rpm for 5 min (25 ± 2 °C). The precipitate was dialyzed (3500 Da) for 72 h and lyophilized using a vacuum freeze dryer (SCIENTZ-10N/E, SCIENTZ, China) for 48 h to obtain EPS powder. The extracted EPS was stored at −20 °C until use. The EPS samples were subjected to protein identification using liquid chromatography-mass spectrometry (LC-MS). Chromatographic separations were performed using an ultra-high performance liquid chromatography system (UPLC, Vanquish Flex, Thermo Scientific, USA). High-resolution mass spectrometry (MS) was conducted using a mass spectrometer (Orbitrap Exploris 120, Thermo Scientific, USA). Protein extraction, enzymatic digestion, peptide extraction, mass spectrometry analysis, and subsequent database matching were performed to analyze the types and relative abundance of amino acids in the EPS proteins.

2.7. EPS and EPS-Fe^{2+} complex characterization

A mixture containing 1 mg EPS and 1 mg $FeCl_2$ was anaerobically mixed to 100 mL sterile EASW medium. The solution was dialyzed (3500 Da) for 24 h and lyophilized. UV–Vis spectroscopy (UV-2550, Shimadzu Corporation, Kyoto, Japan) and FT-IR spectroscopy (Nicolet™ iS™ 5, Thermo Scientific, USA) were employed for characterization. UV–Vis scans covered 200–400 nm, while the FT-IR spectra were acquired across 400–4000 cm^{-1}.

2.8. Corrosion test of EPS

The 7-d immersion and electrochemical test were performed in sterile control and SRB broth following experimental protocols in Sections 2.3 and 2.5. An injection experiment was performed after 3-d biofilm formation. OCP and LPR scans were performed every 20 min before EPS injection in six parallel electrochemical cells. PDP tests were conducted in three parallel electrochemical cells. Then, EPS was injected into another three electrochemical glass cells to achieve 1 g/L and 5 g/L final concentration according to our previous work (Zhang et al., 2025). The glass cell was gently shaken for 5 min. After allowing the OCP to stabilize for 100 s, OCP and LPR scans were performed every 20 min to monitor the

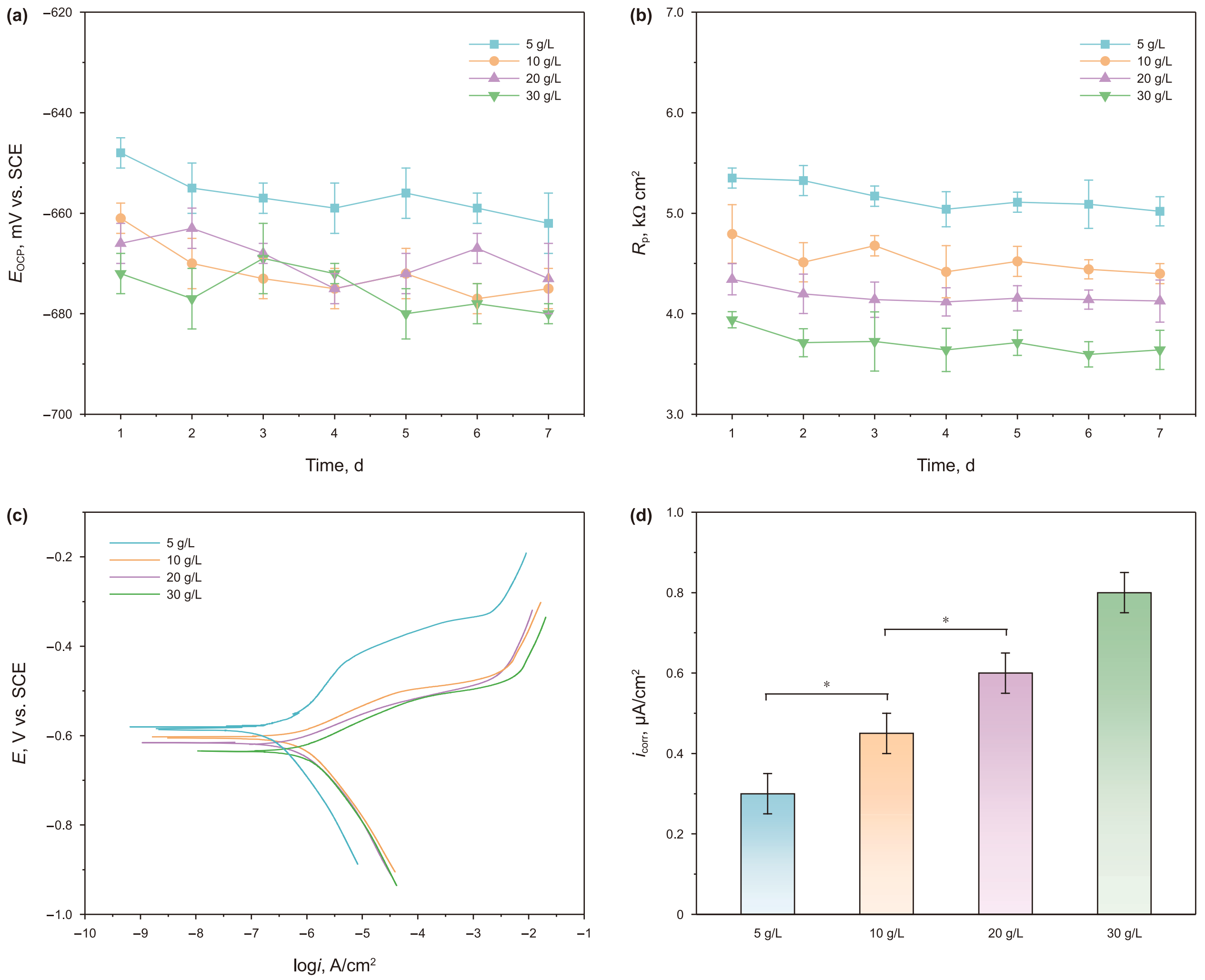

Fig. 2. Electrochemical analysis of chloride concentrations on corrosion of X80 steel in anaerobic sterile EASW medium. **(a)** E_{OCP}, **(b)** R_p, **(c)** potentiodynamic polarization curves, **(d)** i_{corr} calculated from (c). *$P < 0.05$.

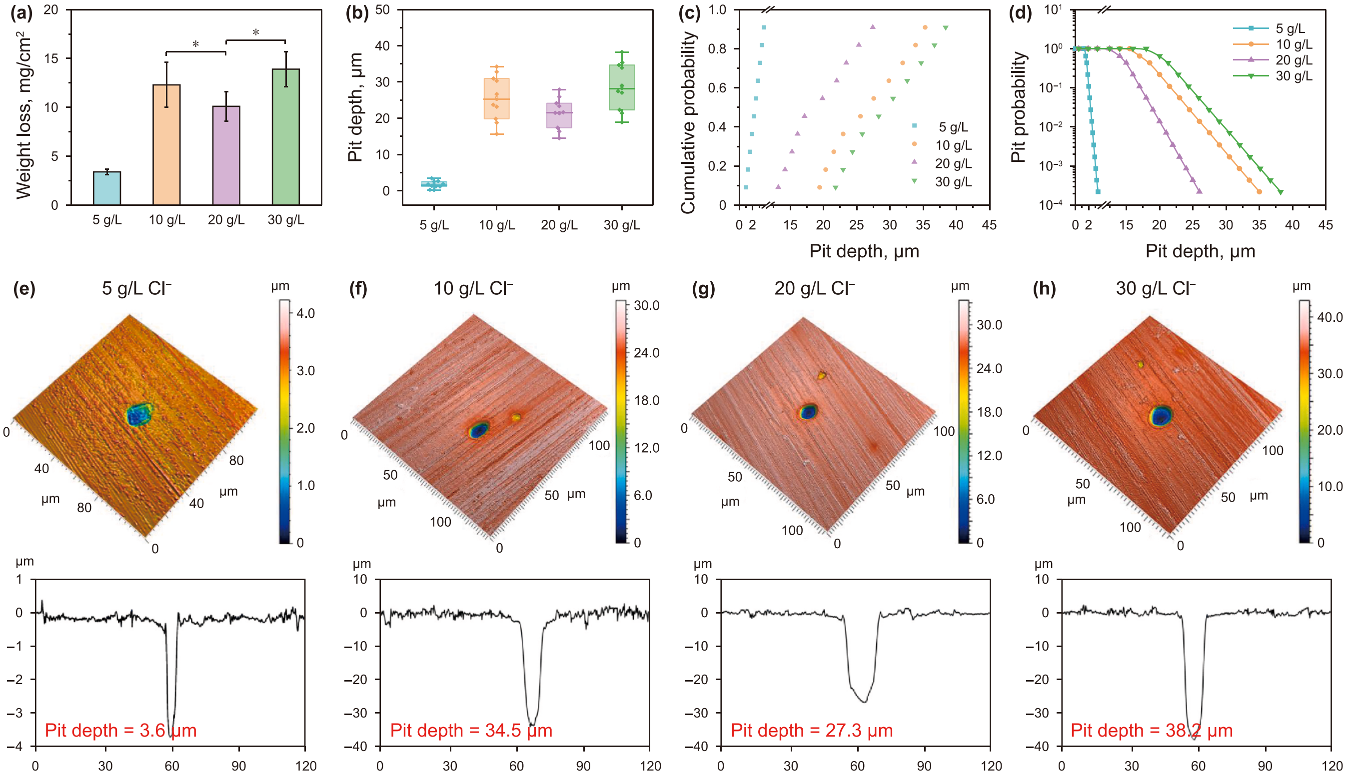

Fig. 3. The effect of chloride concentrations on MIC of X80 steel in EASW medium after 7-d incubation. **(a)** Weight loss, **(b)** the box chart of pit depths, **(c)** the cumulative probability, **(d)** pit probability, **(e)**–**(h)** the maximum pit morphology. $^*P < 0.05$.

changes in E_{OCP} and polarization resistance (R_{p}) in an hour, and PDP tests were also conducted. The experiment was conducted at room temperature (25 ± 2 °C).

3. Results and discussion

3.1. Higher chloride promotes general corrosion of X80 steel

Increasing chloride ion concentration from 5 g/L to 30 g/L caused a 50% increase in sterile weight loss of X80 coupons from 1.2 ± 0.1 mg/cm^2 to 1.8 ± 0.2 mg/cm^2 (Fig. 1(a)). This corrosion acceleration is attributed to the coupling effect of iron oxidation and proton reduction, evidenced by headspace hydrogen accumulation from 0.02 mmol to 0.03 mmol (Fig. 1(b)). Chloride ions slightly promoted pitting (Fig. 1(c)), with maximum pit depth increasing from 2.8 μm to 3.7 μm (Fig. 1(e)–(h)), and severe pitting probability rising proportionally (Fig. 1(d)).

Electrochemical measurements further confirmed the accelerating effect of chloride ions on corrosion. Increasing chloride concentration caused a negatively shift in the E_{OCP} (Fig. 2(a)). The R_{p} inversely proportional to corrosion rate (Yang et al., 2025; Li et al., 2026), decreased significantly in sterile medium. Specifically, R_{p} values declined from 5.0 ± 0.2 kΩ cm^2 (5 g/L) to 4.4 ± 0.1 kΩ cm^2 (30 g/L) after 7 days (Fig. 2(b)). EIS data (Fig. S1) fitted with the equivalent circuit (Fig. S2) revealed progressive charge transfer resistance (R_{ct}) reduction following 5 g/L (28.7 ± 4.1 kΩ cm^2) > 10 g/L (17.4 ± 1.2 kΩ cm^2) > 20 g/L (16.8 ± 1.3 kΩ cm^2) > 30 g/L (7.2 ± 0.5 kΩ cm^2). The increase in chloride ion concentration leads to a decrease in the non-ideal film capacitance (Q_{f}) while increasing the non-ideal electrical double layer capacitance (Q_{dl}). Such variations could be associated with chloride ions compromise the protective adsorption layer (Shen et al., 2024), leading to a greater availability of electrochemically active sites at the metal–electrolyte interface. Moreover, in environments with higher chloride concentrations, the enhanced electrolyte conductivity compresses the electrochemical double layer and lowers the activation energy barrier for charge transfer, thereby promoting electrochemical reactions.

Consistent with these observations, potentiodynamic polarization analyses revealed chloride ion concentration-dependent behavior (Fig. 2(c)). Tafel parameters showed negative shifts in corrosion potential (E_{corr}) and the corrosion current density (i_{corr}) value escalated from 0.32 ± 0.05 μA/cm^2 (5 g/L) to 0.81 ± 0.06 μA/cm^2 (30 g/L), representing a 2.5-fold enhancement in corrosion rate (Fig. 2(d)). Notably, the comparable Tafel slopes (β_{a} and β_{c}) indicate preserved anodic and cathodic reaction mechanisms (Table S2). This mechanistic consistency suggests chloride ions primarily facilitate corrosion via surface activation rather than altering fundamental electrochemical reaction (Vignal et al., 2011).

3.2. Chloride-dependent enhancement of MIC induced by *D. desulfuricans*

The corrosion rate of X80 steel coupons in SRB broth exhibited a non-monotonic dependence on chloride ion concentration. Weight loss measurements followed the order: 30 g/L (13.9 ± 2.1 mg/cm^2) > 10 g/L (12.3 ± 1.6 mg/cm^2) > 20 g/L (10.1 ± 1.3 mg/cm^2) > 5 g/L (3.4 ± 0.3 mg/cm^2) (Fig. 3(a)), contrasting the linear chloride ion concentration-dependent corrosion pattern in sterile control. Pitting analysis corroborated this trend (Fig. 3(b)), with maximum pit depths recorded as 3.6 μm (5 g/L), 34.5 μm (10 g/L), 27.3 μm (20 g/L), and 38.2 μm (30 g/L) in the SRB broth (Fig. 3(e)–(h)). The pitting probability followed 30 g/L > 10 g/L > 20 g/L > 5 g/L (Fig. 3(c) and (d)). The corrosion rate of coupons in SRB broth at 20 g/L chloride exhibited a distinct trough.

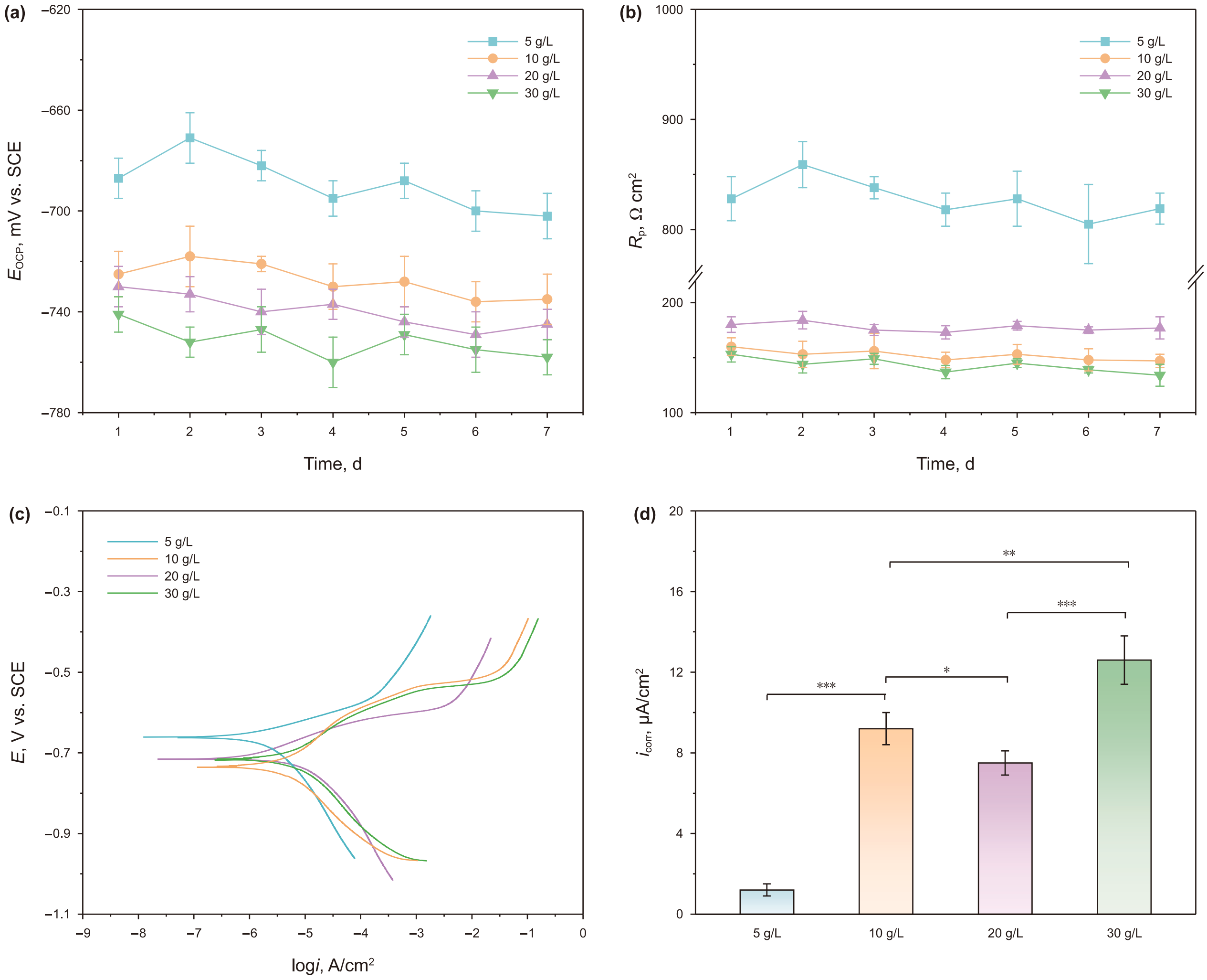

Fig. 4. Electrochemical analysis of chloride concentrations on MIC of X80 steel in EASW medium. **(a)** E_{OCP}, **(b)** R_p, **(c)** potentiodynamic polarization curves, **(d)** i_{corr} calculated from (c). *P < 0.05, **P < 0.01, ***P < 0.001.

The electrochemical data showed E_{OCP} negative shifts with increasing chloride ion concentration in SRB broth (Fig. 4(a)). R_p reached $180.2 \pm 4.1\ \Omega\ \text{cm}^2$ at 20 g/L chloride ion, which was higher 10 g/L ($149.6 \pm 3.3\ \Omega\ \text{cm}^2$) and 30 g/L ($141.3 \pm 2.5\ \Omega\ \text{cm}^2$) (Fig. 4(b)). The highest R_p at 5 g/L chloride ion ($819.6 \pm 13.2\ \Omega\ \text{cm}^2$) aligned with minimal weight loss. R_{ct} obtained from the EIS fitting are consistent with the R_p results (Fig. S3 and Table S3). The order of i_{corr} fitted by PDP curves (Fig. 4(c)) was as follows: 30 g/L ($12.6 \pm 1.2\ \mu\text{A/cm}^2$) > 10 g/L ($9.2 \pm 0.8\ \mu\text{A/cm}^2$) > 20 g/L ($7.5 \pm 0.6\ \mu\text{A/cm}^2$) > 5 g/L ($1.2 \pm 0.3\ \mu\text{A/cm}^2$) (Fig. 4(d)). At 10 g/L and 30 g/L, the anodic Tafel slope exhibited a slight increase, whereas the cathodic Tafel slope decreased significantly (Table S4). This indicates that the cathodic reaction was accelerated, which may be attributed to the enhanced electron uptake capability of SRB under these conditions.

In addition, the pH of the SRB broth remained neutral throughout the experimental period. Therefore, the effect of metabolites-MIC can be considered negligible (Fig. S4).

A comparative analysis of X80 coupons in sterile control and SRB broth revealed that MIC induced by *D. desulfuricans* was more aggressive. As chloride ion concentrations increased from 5 g/L to 30 g/L, the weight loss of coupons in SRB broth exhibited significant enhancement factors of 1.3, 11.9, 8.0, and 10.3 relative to coupons in sterile medium, respectively. The pitting density of the coupons in the SRB broth was much higher than that in the sterile medium (Fig. S5).

The XPS results of the corrosion products are shown in Fig. 5. To gain a more detailed understanding of the corrosion products, the Fe $2p_{3/2}$ spectra were deconvoluted to identify different iron compounds and determine their relative abundances. In sterile medium, the corrosion products consisted of Fe_3O_4 and FeOOH, with their concentrations independent of chloride ion concentration (Fig. 5(a)–(d)). In SRB broth, XPS analysis confirmed the formation of biogenic FeS, consistent with SRB-induced MIC characteristics (Li et al., 2025b). The corrosion products in SRB broth included FeS, Fe_3O_4, and FeOOH, indicating that chloride-mediated MIC acceleration is unrelated to the composition of the corrosion products (Fig. 5(e)–(h)). However, it is noteworthy that the concentrations of the various corrosion products on the sample surface differed in SRB broth with varying chloride ion concentrations. At 20 g/L chloride, the FeS content was highest, whereas at 5 g/L, the FeS content was lowest. This may be related to the effect of chloride ions on SRB metabolism. The detailed mechanisms underlying this chloride-regulated microbial metabolism will be systematically elucidated in the subsequent discussion.

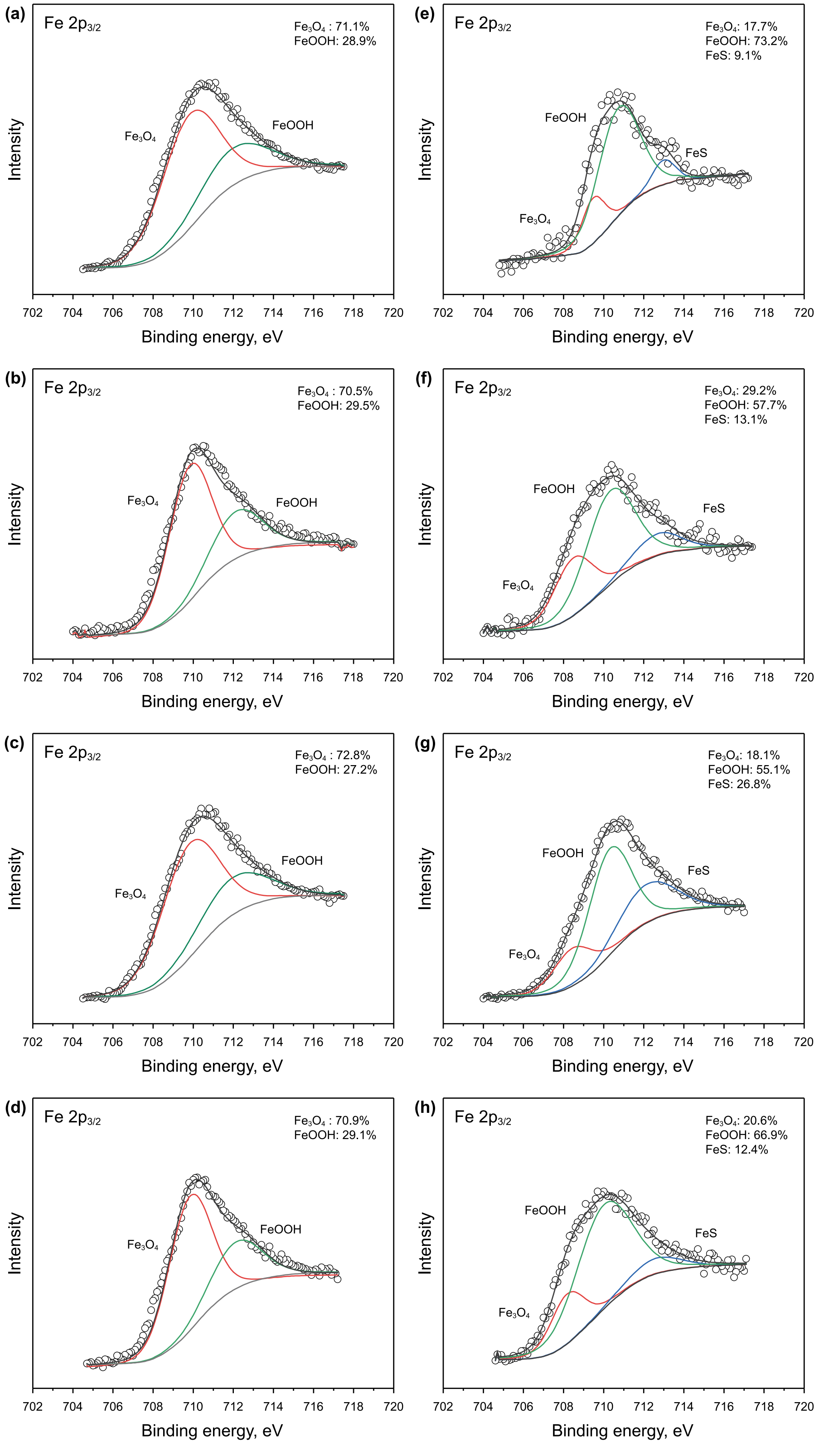

Fig. 5. High-resolution Fe $2p_{3/2}$ XPS spectra of X80 steel after immersed in various medium for 7 d (Sterile medium with **(a)** 5 g/L, **(b)** 10 g/L, **(c)** 20 g/L, and **(d)** 30 g/L chloride. SRB broth with **(e)** 5 g/L, **(f)** 10 g/L, **(g)** 20 g/L, and **(h)** 30 g/L chloride).

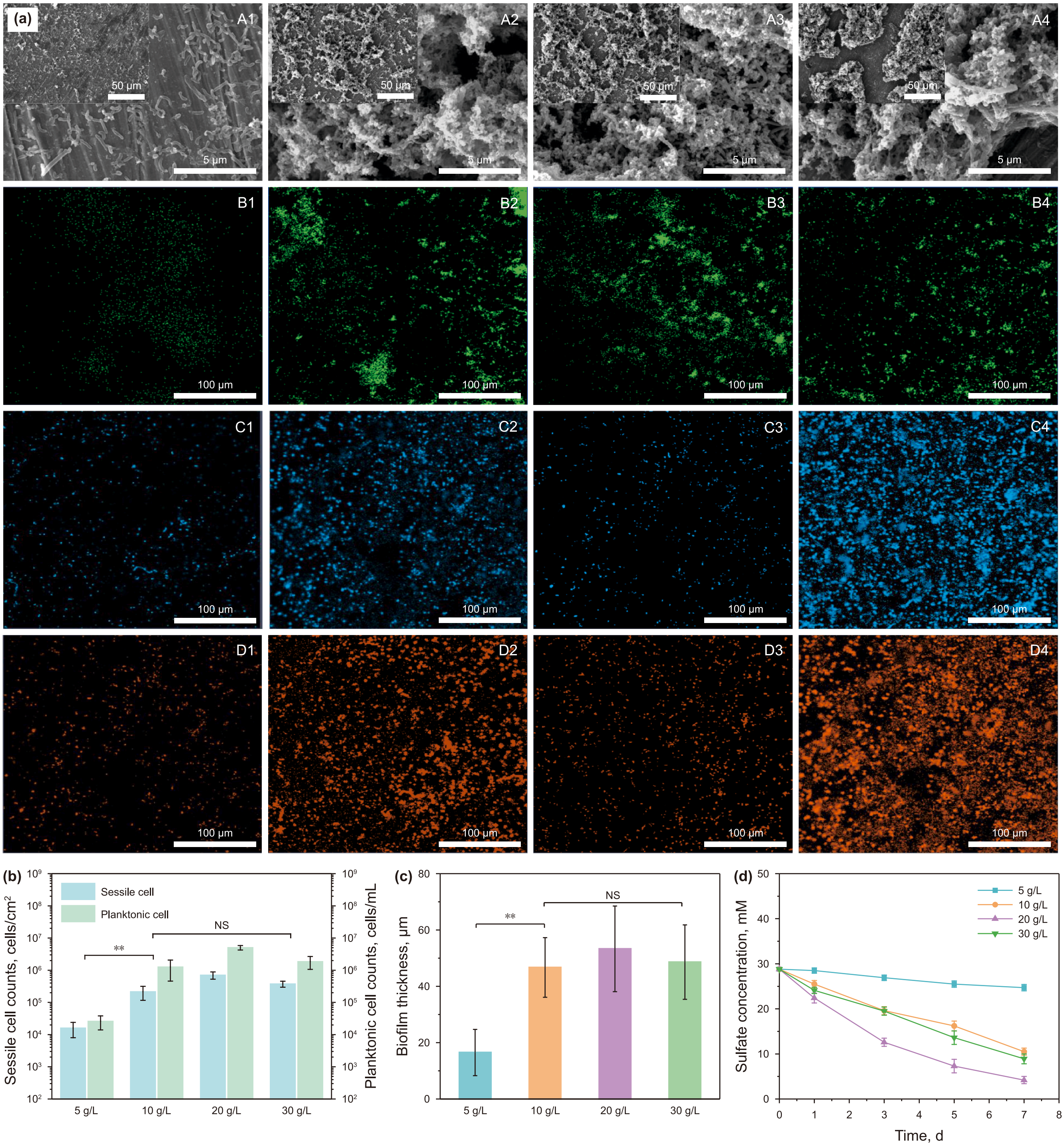

Fig. 6. Biofilms on X80 steel under different conditions. **(a)** Biofilm analysis (A. SEM images of biofilm morphology, B. CLSM images of Biofilm morphology (green), C. CLSM images of proteins (blue), D. CLSM images of polysaccharides (orange). (1) 5 g/L, (2) 10 g/L, (3) 20 g/L, (4) 30 g/L), **(b)** planktonic and sessile cell counts, **(c)** biofilm thickness, and **(d)** sulfate reduction. **$p < 0.01$, NS means $p > 0.05$.

3.3. *Suboptimal chloride environment stimulate EPS production in D. desulfuricans*

The growth curve shows that SRB cells were in the logarithmic and stationary phases during the experimental period (Fig. S6). The cell morphology of *D. desulfuricans* does not exhibit significant differences across different environments, with the cells consistently adopting a short rod-shaped, curved morphology. This uniformity in shape suggests that the environmental conditions, within the range studied, may not exert a significant influence on the overall cellular form (Xiong and Guo, 2011). However, there are significant differences in the biofilm morphology. At 5 g/L chloride ions, sparse cell attachment occurred on coupons surface (Fig. 6(a), A1), whereas 10–30 g/L chloride ions promoted well-

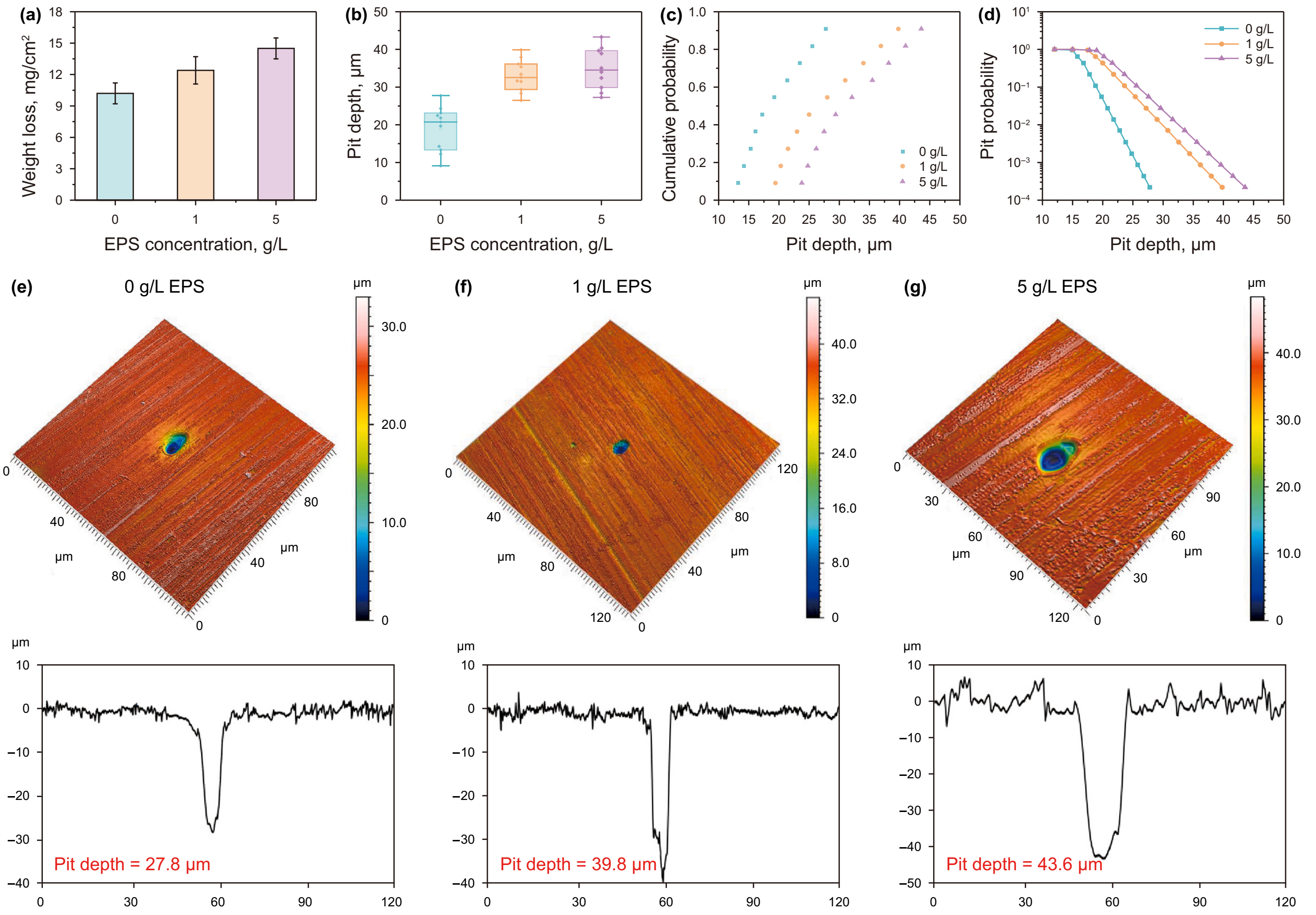

Fig. 7. The effect of EPS concentrations on MIC of X80 steel in biotic EASW medium after 7-d incubation. **(a)** Weight loss, **(b)** the box chart of pit depths, **(c)** the cumulative probability, **(d)** pit probability, **(e)**–**(g)** the maximum pit morphology.

structured and dense biofilms (Fig. 6(a), A2–A4)). Sessile/planktonic cell densities in 10–30 g/L chloride ions media were 100-fold higher than at 5 g/L chloride ion (Fig. 6(b)). Furthermore, biofilm thickness exceeded 40 μm in 10–30 g/L chloride ion double that at 5 g/L (Fig. 6(c)). Sulfate is the sole electron acceptor in the medium, sulfate reduction analysis revealed optimal metabolic activity at 20 g/L, whereas its sulfate-reducing capacity was attenuated at 10 and 30 g/L (Fig. 6(d)). It is noteworthy that sulfate reduction under 5 g/L chloride concentration exhibited a reduction of nearly 85% (4.1 ± 0.5 mM) compared to the 20 g/L condition (24.5 ± 1.2 mM over 7 days), which aligns with the observed lower cell counts.

EPS component analysis showed pronounced polysaccharide/protein accumulation at 10 g/L and 30 g/L chloride ion (Fig. 6(a), C2, C4, D2 and D4)), contrasting minimal signals in other conditions. Polysaccharides and proteins are key constituents of EPS that are essential for maintaining biofilm structural integrity and functionality (Xu et al., 2022; Lou et al., 2023). Prior studies indicated that environmental stressors (e.g., non-optimal temperatures, nutrient limitations, and osmotic stress) trigger EPS biosynthesis as a survival strategy (Bi et al., 2024; Wu et al., 2025). The microbial cells redirect metabolic resources from replication to EPS-mediated osmoprotection under suboptimal chloride environments. The enhanced exopolysaccharide layer protects the cells from dehydration by creating a microenvironment around the cell wall that buffers osmotic imbalance across the cell membrane, provides a reservoir of water for the cells, and slows down ion influx under low-salinity conditions (Sheng et al., 2006). This polymeric matrix not only facilitates metabolic sustenance but also potentially accelerates MIC. The pronounced EPS production in suboptimal chloride environments likely constitutes the primary mechanism underlying the observed MIC rate enhancement.

3.4. *EPS is a major intermediate in MIC induced by D. desulfuricans*

3.4.1. *Effect of EPS on the corrosion behavior*

To evaluate the role of EPS in MIC, we isolated and purified EPS from SRB broth. The purified EPS was introduced into SRB broth at concentrations of 0, 1, and 5 g/L followed by a 7-day corrosion assessment. Weight loss analysis revealed a direct correlation between EPS and MIC (Fig. 7(a)). Specifically, coupons exhibited progressively higher weight loss of 10.2 ± 0.9 mg/cm^2 (0 g/L EPS), 12.4 ± 1.3 mg/cm^2 (1 g/L EPS), and 14.5 ± 1.1 mg/cm^2 (5 g/L EPS), respectively. Maximum pit depths increased substantially from 27.8 μm in EPS-free medium to 39.8 μm and 43.6 μm at 1 g/L and 5 g/L EPS, respectively (Fig. 7(e)–(g)). Pitting probability followed a concentration-dependent hierarchy: 5 g/L > 1 g/L > 0 g/L (Fig. 7(c) and (d)).

Electrochemical test showed the addition of EPS had little effect on E_{OCP} (Fig. 8(a)). The addition of 5 g/L EPS caused a 30% reduction in R_p value, decreased form 180.4 Ω cm^2 (0 g/L) to 121.2 Ω cm^2 (5 g/L) (Fig. 8(b)). Consistently, the EIS fitted results revealed a

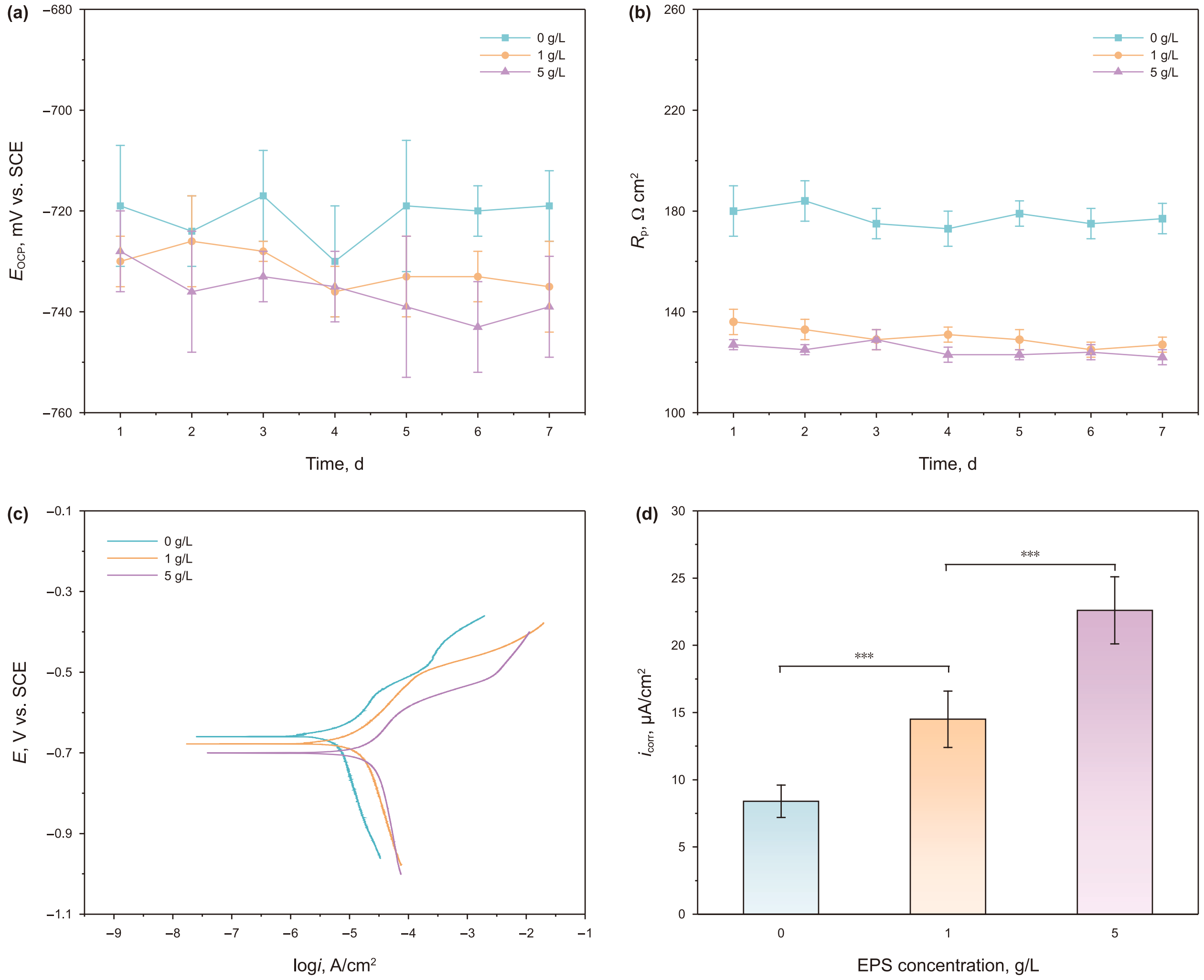

Fig. 8. Electrochemical analysis of the EPS on MIC of X80 steel in SRB broth. **(a)** E_{OCP}, **(b)** R_p, **(c)** potentiodynamic polarization curves, **(d)** i_{corr} calculated from (c). ***$P < 0.001$.

significant decline in R_{ct} with EPS addition (Fig. S7 and Table S5). Tafel analysis confirmed i_{corr} values were 8.4 ± 1.2 μA/cm^2 (0 g/L), 14.5 ± 2.1 μA/cm^2 (1 g/L), and 22.6 ± 2.5 μA/cm^2 (5 g/L), respectively (Fig. 8(c) and (d)). All electrochemical data indicated EPS accelerated MIC. Supplementary electrochemical analyses under sterile control conditions revealed EPS slightly enhanced corrosion of X80 coupons (Fig. S8). The addition of 5 g/L EPS induced a 10% decrease in R_p from 960 Ω cm^2 (EPS-free) to 850 Ω cm^2, accompanied by a marginal increase in i_{corr} from 0.6 μA/cm^2 (EPS-free) to 0.7 μA/cm^2 (5 g/L). This marked contrast between biotic and sterile systems implies that the EPS-mediated corrosion enhancement might be mechanistically linked to the distinctive EET processes inherent to MIC.

3.4.2. *EPS accelerates corrosion through complexation of ferrous ion*

LC-MS was used to analyze the types and relative abundance of amino acids in the EPS proteins. The EPS proteins contain a variety of amino acids, including alanine, glutamic acid, isoleucine, leucine, tyrosine, and others (Fig. 9(a)). The ferrous ion complexation capacity of EPS was systematically investigated through UV–Vis and FT-IR spectroscopic analyses (Fig. 9(b) and (c)). UV–Vis spectra of EPS exhibited two characteristic absorption bands. The 200–210 nm band corresponding to $n \rightarrow \pi^*$ transitions in protein amide bonds and oxygen-containing functional groups (carboxyl, carbonyl, esters) (Yun and Park, 2003), and a 250–280 nm band associated with $\pi \rightarrow \pi^*$ transitions in aromatic/polyaromatic compounds (Jia et al., 2007). The UV–Vis spectral profiles remained unaffected by the presence of free Fe^{2+} ions in solution. Upon Fe^{2+} complexation, critical spectral modifications occurred: the attenuation of the absorption peak at 200–210 nm suggests the formation of coordination bonds between Fe^{2+} and unsaturated moieties (C═O, N═O). The C═O bond may be related to the structures in glutamic acid and aspartic acid, while the N═O bond may be associated with the nitroso groups in cysteine, histidine, and arginine. Additionally, a bathochromic shift in the 250–280 nm region, attributed to reduced $\pi \rightarrow \pi^*$ transition energy barriers resulting from interactions between Fe^{2+} d-orbitals and aromatic π-systems in EPS (Abu et al., 1991; Kılınççeker and Baş, 2020). This electronic modulation arises from π–π/p–π conjugation effects that redistribute electron density toward electronegative O/N atoms, thereby endowing EPS with metal ion complexation capabilities through both electrostatic interactions and chemical coordination bonds (Kaczmarczyk, 2013).

In both EPS and EPS–Fe^{2+} complex, multiple distinct spectral bands were observed. The peak at 3300 cm^{-1} corresponds to the O–H stretching vibration of alcohols, phenols, or organic acids. The peak at approximately 2830 cm^{-1} originates from the

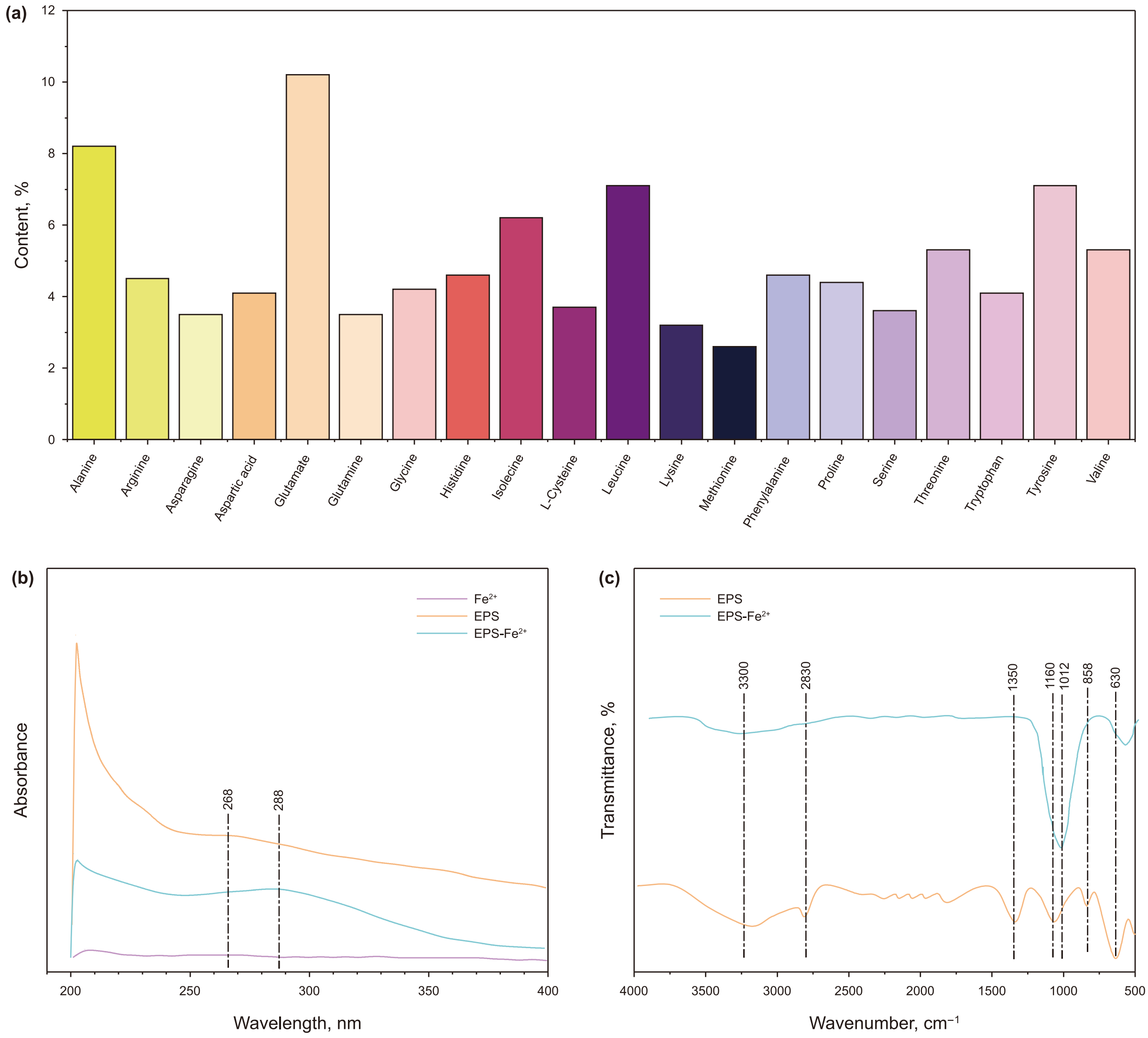

Fig. 9. Characterization of EPS and Fe^{2+} complex. **(a)** LC-MS analysis of amino acid in the EPS, **(b)** UV–Vis and **(c)** FT-IR spectra of EPS and EPS-Fe^{2+} complex.

asymmetric stretching vibration of $-CH_2$ in the macromolecular polysaccharides of EPS; the region between 1700 and 1200 cm^{-1} is attributed to protein signatures, including amide I (C=O stretching vibration related to glutamic acid and aspartic acid, 1700–1600 cm^{-1}), amide II (N–H bending related to Glutamine Lysine and Arginine, or C–N stretching related to Glutamic acid, Tryptophan and Tyrosine, 1600–1500 cm^{-1}), and amide III (C–N/C–O vibrations, 1300–1200 cm^{-1}). The C–O bond is associated with glutamic acid, aspartic acid, tyrosine, serine, and threonine. The range of 1200–900 cm^{-1} belongs to the polysaccharide/nucleic acid vibration region, where the peak at 1160 cm^{-1} corresponds to the stretching vibration of C–O from COO^- or P=O. The P=O bond is associated with Serine, Threonine and Tyrosine. The region of 900–600 cm^{-1} is assigned to the fingerprint zone (Omoike and Chorover, 2004; Yuan et al., 2011; Wu et al., 2022). Upon complexation of EPS with Fe^{2+}, the peak at 2830 cm^{-1} disappeared, indicating an interaction between Fe^{2+} and polysaccharides. Additionally, a slight redshift was observed in the peak at 1160 cm^{-1}, which was attributed to the interaction between Fe^{2+} and active functional groups (COO^- or P=O), leading to the formation of C–O–Fe or P–O–Fe bonds. The FT-IR and UV–Vis results collectively confirmed the formation of a coordination complex between Fe^{2+} and EPS.

The anodic reaction of steel ($Fe \rightarrow Fe^{2+} + 2e^-$) is a core step in metal corrosion, and its rate directly determines the overall corrosion process. EPS forms stable complexes with Fe^{2+}, significantly reducing the concentration of free Fe^{2+} in the solution. According to Le Chatelier's principle, the equilibrium of the anodic reaction shifts toward the product side (to the right), forcing more metallic iron to dissolve to compensate for the complexed Fe^{2+}, thereby accelerating the rate of the anodic reaction. In contrast, the corrosion rate of X80 coupons in sterile medium were slower (Fig. 1), yielding comparatively lower Fe^{2+} concentrations, thus EPS demonstrated minimal enhancement effects on sterile corrosion (Fig. S8).

3.4.3. EPS as an electron shuttle accelerates the EET-MIC

Electroactive bacteria can utilize EPS to promote MIC through electron shuttles mediated EET. To validate the role of EPS as an electron shuttle, short-term injection tests were conducted to avoid interference from cell proliferation and Fe^{2+}-EPS complexation. The electrochemical responses of X80 steel electrodes were

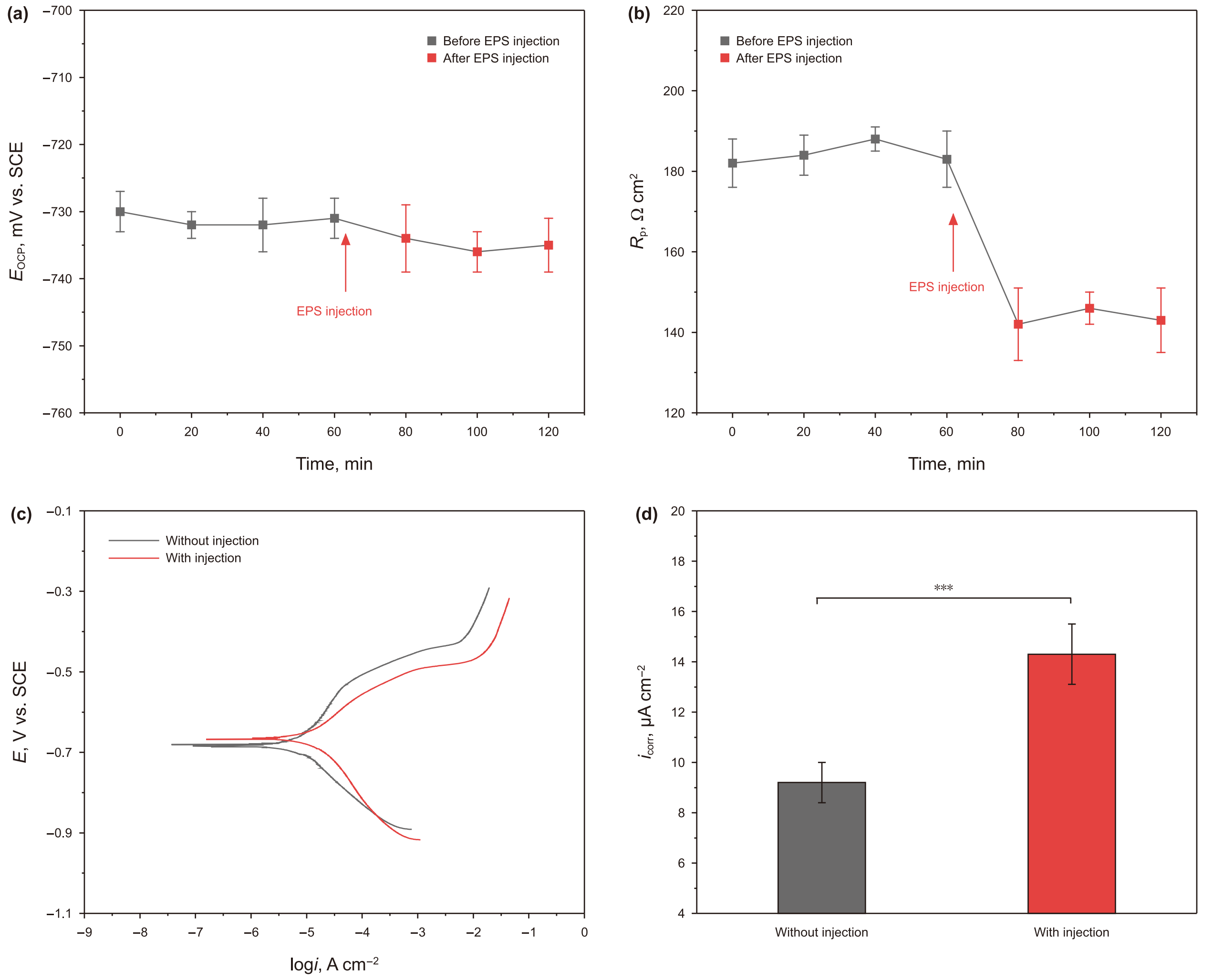

Fig. 10. The electrochemical response of X80 steel coupons in the medium after the injection of 1 g/L EPS. **(a)** E_{OCP}, **(b)** R_p, **(c)** potentiodynamic polarization curves, and **(d)** i_{corr} calculated from (c). ***P < 0.001.

monitored after the injection of 1 g/L EPS. Compared to the control group without EPS, the E_{OCP} exhibited no significant variation within 2 h after injection (Fig. 10(a)). However, the R_p decreased from 182 ± 7 Ω cm^2 to 143 ± 6 Ω cm^2 (Fig. 10(b)), while the i_{corr} increased from 9.2 ± 0.8 μA/cm^2 to 14.3 ± 1.2 μA/cm^2 (Fig. 10(c) and (d)). These results demonstrate that EPS injection instantaneously enhances MIC, aligning with the characteristics of electron shuttles mediated EET-MIC mechanisms.

In the context of EET-MIC, metallic iron can act as an electron donor to energize SRB growth according to the biocatalytic cathodic sulfate reduction theory (25 °C, 1 M solute and pH 7) (Li et al., 2018):

$$Fe \rightarrow Fe^{2+} + 2e^- \ (E^\circ = -447 \text{ mV vs. SHE}) \tag{1}$$

$$CH_3CHOHCOO^- + 2H_2O \rightarrow 2CH_3COO^- + CO_2 + 8H^+ + 8e^- \ (E^{\circ\prime} = -430 \text{ mV vs. SHE}) \tag{2}$$

$$SO_4^{2-} + 9H^+ + 8e^- \rightarrow HS^- + 4H_2O \ (E^{\circ\prime} = -217 \text{ mV vs. SHE}) \tag{3}$$

when the SRB cells utilize soluble electron donors, such as lactate, nutrients diffuse into the cytoplasm to fuel respiratory metabolism. However, electrons derived from metallic iron (an insoluble solid) cannot be directly transferred into microbial cells; they require the assistance of electron shuttles, *c*-type outer-membrane cytochromes, or conductive nanowires to facilitate the electron transfer process. Notably, due to the single-step tunneling limit, the distance between the protein active centers and the electron acceptors/donors should be less than 2 nm (Gray and Winkler, 2005). Consequently, the micrometer-scale thickness of the EPS layer would inherently impede direct electron transfer between bacteria and the metal surface. Nevertheless, EPS primarily consists of polysaccharides, proteins, glycoproteins, glycolipids, humic substances, and extracellular DNA (Young et al., 2006; Sheng et al., 2010). These redox-active molecules confer electron-shuttling properties to EPS. Previous studies have confirmed that extracellular enzymes within EPS can act as biocatalysts to accelerate steel corrosion (Liu et al., 2017). Additionally, hydrated polysaccharides or conductive polymers have been employed to enhance the conductivity of electroactive materials (Finkenstadt, 2005). FT-IR results verify the presence of redox-active functional groups in EPS. These functional groups can adsorb and/or bind secreted redox-active molecules, consistent with the characteristics of electron shuttles mediating EET-MIC. Therefore, under suboptimal chloride environments, *D. desulfuricans* secretes EPS as electron shuttles to facilitate electron transfer between the metal and microbial cells, thereby accelerating MIC.

4. Conclusions

This study elucidates the regulatory mechanism of chloride ions in the MIC of X80 steel induced by *D. desulfuricans*. The results demonstrate that the sterile corrosion rate of X80 steel is positively correlated with chloride ion concentration. In SRB broth, the MIC rate was significantly higher than the sterile corrosion rate, with the following order: 30 g/L > 10 g/L > 20 g/L > 0 g/L Cl^-. This difference arises from the bacterial adaptation to varying chloride ion concentrations, which triggers EPS secretion and specifically accelerates MIC. Experiments with exogenous EPS injection confirmed its role as an electron shuttle. Furthermore, the EPS-Fe^{2+} complex establishes a synergistic mechanism for corrosion acceleration. These findings collectively suggest that chloride ion regulation of *D. desulfuricans* metabolism, particularly through EPS biosynthesis, is a key driving factor in MIC enhancement. The detection of EPS produced by SRB may become a critical method for MIC detection in the future, and the elimination of EPS could serve as an effective strategy to control MIC in marine environments. This research direction offers significant potential for the development of monitoring and detection technologies for MIC in marine environments. Future work could further identify the active components in EPS secreted by different microorganisms that control EET, providing more precise targets for mitigation strategies.

CRediT authorship contribution statement

Jia-Hang Li: Writing – review & editing, Writing – original draft, Visualization, Validation, Methodology, Investigation, Formal analysis, Data curation, Conceptualization. **En-Ze Zhou:** Writing – review & editing, Validation, Project administration, Methodology, Funding acquisition, Formal analysis. **Zhong Li:** Writing – review & editing. **Di Wang:** Writing – review & editing. **Fu-Hui Wang:** Project administration. **Da-Ke Xu:** Project administration, Funding acquisition.

Declaration of interest statement

The authors declare that they have no known competing financial interests or personal relationships that could have appeared to influence the work reported in this paper.

Acknowledgements

This work is financially supported by the National Science Fund for Distinguished Young Scholars (Grant No. 52425112), National Natural Science Foundation of China (Grant No. U24A2032), National Key Research and Development Program of China (Grant No. 2022YFB3808800), Guangdong Basic and Applied Basic Research Foundation (Grant No. 2023A1515240080), Young Elite Scientists Sponsorship Program by CAST (Grant No. 2022QNRC001), Fundamental Research Funds for the Central Universities (Grant No. 2023-MSBA-040), Research Fund of National Key Laboratory of Marine Corrosion and Protection of Luoyang Ship Material Research Institute (Grant No. GJK2402).

Supplementary data

Supplementary data to this article can be found online at https://doi.org/10.1016/j.petsci.2025.12.004.

References

Abu, G.O., Weiner, R.M., Rice, J., et al., 1991. Properties of an extracellular adhesive polymer from the marine bacterium, *Shewanella Colwelliana*. Biofouling 3 (1), 69–84. https://doi.org/10.1080/08927019109378163.

ASTM Standard, ASTM G1–25, 2025. Standard Practice for Preparing, Cleaning, and Evaluating Corrosion Test Specimens. https://doi.org/10.1520/G0001-25.

Bharti, N., Barnawal, D., Maji, D., et al., 2015. Halotolerant pgprs prevent major shifts in indigenous microbial community structure under salinity stress. Microb. Ecol. 70 (1), 196–208. https://doi.org/10.1007/s00248-014-0557-4.

Bi, Y.L., Tan, H., Zhang, S.S., et al., 2024. Response mechanism of extracellular polymeric substances synthesized by *Alternaria* sp. on drought stress in alfalfa (*Medicago sativa* L.). J. Agric. Food Chem. 72 (30), 16812–16824. https://doi.org/10.1021/acs.jafc.4c04009.

Chakraborty, S., Mondal, S., 2023. Halotolerant *Citrobacter* sp. remediates salinity stress and promotes the growth of Vigna radiata (L) by secreting extracellular polymeric substances (EPS) and biofilm formation: A novel active cell for microbial desalination cell (MDC). Int. Microbiol. 27, 291–301. https://doi.org/10.1007/s10123-023-00386-6.

Dong, B.J., Liu, W., Zhang, T.Y., et al., 2023. Clarifying the effect of a small amount of Cr content on the corrosion of Ni-Mo steel in tropical marine atmospheric environment. Corros. Sci. 210, 110813. https://doi.org/10.1016/j.corsci.2022.110813.

Finkenstadt, V.L., 2005. Natural polysaccharides as electroactive polymers. Appl. Microbiol. Biotechnol. 67 (6), 735–745. https://doi.org/10.1007/s00253-005-1931-4.

Forni, C., Duca, D., Glick, B.R., 2017. Mechanisms of plant response to salt and drought stress and their alteration by rhizobacteria. Plant Soil 410 (1), 335–356. https://doi.org/10.1007/s11104-016-3007-x.

Fu, M.Y., Cheng, X., Li, J.R., et al., 2023. Influence of soluble, loosely bound and tightly bound extracellular polymeric substances (EPS) produced by *Desulfovibrio vulgaris* on EH40 steel corrosion. Corros. Sci. 221, 111342. https://doi.org/10.1016/j.corsci.2023.111342.

Gao, Y., Zhang, M.X., Fan, Y.Q., et al., 2022. Marine *Vibrio* spp. protect carbon steel against corrosion through secreting extracellular polymeric substances. npj Mat. Degrad. 6, 6. https://doi.org/10.1038/s41529-021-00212-2.

Gao, Y., Zhang, J.R., Wang, D.L., et al., 2024. Naturally effective inhibition of microbial corrosion on carbon steel by beneficial biofilm in the South China Sea. Colloid Interface Sci. 59, 100779. https://doi.org/10.1016/j.colcom.2024.100779.

Gray, H.B., Winkler, J.R., 2005. Long-range electron transfer. P. Natl. Acad. Sci. USA. 102 (10), 3534–3539. https://doi.org/10.1073/pnas.0408029102.

Hao, X.P., Bai, Y., Ren, C.H., et al., 2022. Self-healing effect of damaged coatings via biomineralization by *Shewanella putrefaciens*. Corros. Sci. 196, 110067. https://doi.org/10.1016/j.corsci.2021.110067.

He, J.Q., Tan, Y., Liu, H.X., et al., 2022. Extracellular polymeric substances secreted by marine fungus *Aspergillus terreus*: Full characterization and detailed effects on aluminum alloy corrosion. Corros. Sci. 209, 110703. https://doi.org/10.1016/j.corsci.2022.110703.

Isfahani, F.M., Tahmourespour, A., Hoodaji, M., et al., 2018. Characterizing the new bacterial isolates of high yielding exopolysaccharides under hypersaline conditions. J. Clean. Prod. 185, 922–928. https://doi.org/10.1016/j.jclepro.2018.03.030.

Jia, S.R., Yu, H.F., Lin, Y.X., et al., 2007. Characterization of extracellular polysaccharides from *Nostoc flagelliforme* cells in liquid suspension culture. Biotechnol. Bioproc. Eng. 12 (3), 271–275. https://doi.org/10.1007/BF02931103.

Kaczmarczyk, B., 2013. FTIR studies on protonation of selected aromatic polyimines. J. Mol. Struct. 1054–1055, 223–227. https://doi.org/10.1016/j.molstruc.2013.09.028.

Kılınççeker, G., Baş, M., 2020. The inhibition effect of (E)-2-Hydroxy-5-(2-benzylidene) aminobenzoic acid on corrosion behaviour of mild steel in 1.0 M HCl solution. Prot. Met. Phys. Chem. 56 (2), 414–426. https://doi.org/10.1134/S2070205120020112.

Li, Y.C., Xu, D.K., Chen, C.F., et al., 2018. Anaerobic microbiologically influenced corrosion mechanisms interpreted using bioenergetics and bioelectrochemistry: A review. J. Mater. Sci. Technol. 34 (10), 1713–1718. https://doi.org/10.1016/j.jmst.2018.02.023.

Li, S.L., Qu, Q., Li, L., et al., 2019. *Bacillus cereus* s-EPS as a dual bio-functional corrosion and scale inhibitor in artificial seawater. Water Res. 166, 115094. https://doi.org/10.1016/j.watres.2019.115094.

Li, Z., Wang, J., Dong, Y.Z., et al., 2021. Synergistic effect of chloride ion and *Shewanella algae* accelerates the corrosion of Ti-6Al-4V alloy. J. Mater. Sci. Technol. 71, 177–185. https://doi.org/10.1016/j.jmst.2020.07.022.

Li, J.H., Zhou, E.Z., Xie, F., et al., 2025a. Accelerated stress corrosion cracking of X80 pipeline steel under the combined effects of sulfate-reducing bacteria and hydrostatic pressure. Corros. Sci. 243, 112593. https://doi.org/10.1016/j.corsci.2024.112593.

Li, J.H., Wang, D., Ouyang, X., et al., 2026. Bifunctional eco-friendly tobacco stem extract with antibacterial and corrosion inhibition properties for mitigating microbiologically influenced corrosion. J. Mater. Sci. Technol. 257, 46–59. https://doi.org/10.1016/j.jmst.2025.09.011.

Li, Y.Y., Wang, B.B., Wang, Y., et al., 2025b. Beneficial effect of heat input to improve microbial corrosion resistance of welded joint in X80 steel pipeline. J. Mater. Sci. Technol. 223, 217–234. https://doi.org/10.1016/j.jmst.2024.10.034.

Little, B.J., Blackwood, D.J., Hinks, J., et al., 2020. Microbially influenced corrosion-any progress? Corros. Sci. 170, 108641. https://doi.org/10.1016/j.corsci.2020.108641.

Liu, H.W., Gu, T.Y., Asif, M., et al., 2017. The corrosion behavior and mechanism of carbon steel induced by extracellular polymeric substances of iron-oxidizing bacteria. Corros. Sci. 114, 102–111. https://doi.org/10.1016/j.corsci.2016.10.025.

Liu, H.W., Chen, C.Y., Asif, M., et al., 2022a. Mechanistic investigations of corrosion and localized corrosion of X80 steel in seawater comprising sulfate-reducing bacteria under continuous carbon starvation. Corros. Commun. 8, 70–80. https://doi.org/10.1016/j.corcom.2022.08.002.

Liu, H.X., Chen, W., Tan, Y., et al., 2022b. Characterizations of the biomineralization film caused by marine *Pseudomonas stutzeri* and its mechanistic effects on X80 pipeline steel corrosion. J. Mater. Sci. Technol. 125, 15–28. https://doi.org/10.1016/j.jmst.2022.02.033.

Liu, B.B., Govindan, R., Muthuchamy, M., et al., 2022c. *Halophilic archaea* and their extracellular polymeric compounds in the treatment of high salt wastewater containing phenol. Chemosphere 294, 133732. https://doi.org/10.1016/j.chemosphere.2022.133732.

Lou, Y.T., Chang, W.W., Cui, T.Y., et al., 2023. Microbiologically influenced corrosion inhibition induced by *S. putriefaciens* mineralization under extracellular polymeric substance regulation via FlrA and FlhG genes. Corros. Sci. 221, 111350. https://doi.org/10.1016/j.corsci.2023.111350.

Meneses, C., Gonçalves, T., Alquéres, S., et al., 2017. *Gluconacetobacter diazotrophicus* exopolysaccharide protects bacterial cells against oxidative stress in vitro and during rice plant colonization. Plant Soil 416 (1), 133–147. https://doi.org/10.1007/s11104-017-3201-5.

Morra, R., Carratore, F.D., Muhamadali, H., et al., 2018. Translation stress positively regulates mscl-dependent excretion of cytoplasmic proteins. mBio 9 (1), e02118-17. https://doi.org/10.1128/mBio.02118-17.

Niu, G., Yuan, R., Wang, E., et al., 2024. Unraveling the influence of Mo on the corrosion mechanism of Ni-advanced weathering steel in harsh marine atmospheric environments. J. Mater. Sci. Technol. 195, 41–62. https://doi.org/10.1016/j.jmst.2024.02.021.

Omoike, A., Chorover, J., 2004. Spectroscopic study of extracellular polymeric substances from *Bacillus subtilis*: Aqueous chemistry and adsorption effects. Biomacromolecules 5 (4), 1219–1230. https://doi.org/10.1021/bm034461z.

Shen, F.M., Li, M.H., Liu, G.J., et al., 2024. Unveiling the intricacies of steel corrosion induced by chloride: insights from reactive molecular dynamics simulation. Constr. Build. Mater. 443, 137839. https://doi.org/10.1016/j.conbuildmat.2024.137839.

Sheng, G.P., Yu, H.Q., Yue, Z., 2006. Factors influencing the production of extracellular polymeric substances by *Rhodopseudomonas acidophila*. Int. Biodeterior. Biodegrad. 58 (2), 89–93. https://doi.org/10.1016/j.ibiod.2006.07.005.

Sheng, G.P., Yu, H.Q., Li, X.Y., 2010. Extracellular polymeric substances (EPS) of microbial aggregates in biological wastewater treatment systems: A review. Biotechnol. Adv. 28 (6), 882–894. https://doi.org/10.1016/j.biotechadv.2010.08.001.

Tuck, B., Watkin, E., Somers, A., et al., 2022. A critical review of marine biofilms on metallic materials. npj Mater. Degrad. 6 (1), 25. https://doi.org/10.1038/s41529-022-00234-4.

Ueki, T., Lovley, D.R., 2022. *Desulfovibrio vulgaris* as a model microbe for the study of corrosion under sulfate-reducing conditions. mLife 1 (1), 13–20. https://doi.org/10.1002/mlf2.12018.

Vignal, V., Zhang, H., Delrue, O., et al., 2011. Influence of long-term ageing in solution containing chloride ions on the passivity and the corrosion resistance of duplex stainless steels. Corros. Sci. 53 (3), 894–903. https://doi.org/10.1016/j.corsci.2010.11.011.

Wang, Q., Wang, B.B., Zhou, X.B., et al., 2024a. Effects of carbon source starvation and riboflavin addition on selective corrosion of welded joint by *Desulfovibrio vulgaris*. Corros. Sci. 230, 111931. https://doi.org/10.1016/j.corsci.2024.111931.

Wang, D., Ueki, T., Ma, P., et al., 2024b. Chloride enhances corrosion associated with sulfate-reducing bacteria. Corros. Sci. 233, 112096. https://doi.org/10.1016/j.corsci.2024.112096.

Wu, D.Q., Ding, X.S., Zhao, B., et al., 2022. The essential role of hydrophobic interaction within extracellular polymeric substances in auto-aggregation of *P. stutzeri* strain XL-2. Int. Biodeterior. Biodegrad. 171, 105404. https://doi.org/10.1016/j.ibiod.2022.105404.

Wu, Z.C., Kang, J., Mao, L.Y., et al., 2025. Deciphering bioprocess responses in organic phosphorus mineralization to different antibiotic stresses: Interaction mechanisms mediated by microbial succession and extracellular polymeric substances and regulatory patterns. Bioresour. Technol. 417, 131874. https://doi.org/10.1016/j.biortech.2024.131874.

Xiao, Y., Zhang, E., Zhang, J., et al., 2017. Extracellular polymeric substances are transient media for microbial extracellular electron transfer. Sci. Adv. 3 (7), e1700623. https://doi.org/10.1126/sciadv.1700623.

Xie, F., Guo, Z.W., Wang, D., et al., 2019. Synergistic effect between chloride and sulfate reducing bacteria in corrosion inhibition of X100 pipeline steel in Marine environment. Int. J. Electrochem. Sci. 14 (3), 2693–2704. https://doi.org/10.20964/2019.03.54.

Xie, F., Wang, Y.X., Wang, D., et al., 2023. Influence of anion and sulfate-reducing bacteria on the stress corrosion behavior and mechanism of X70 steel in a marine mud environment. Eng. Fail. Anal. 143, 106834. https://doi.org/10.1016/j.engfailanal.2022.106834.

Xiong, H.X., Guo, R., 2011. Effects of chloride acclimation on iron oxyhydroxides and cell morphology during cultivation of acidithiobacillus ferrooxidans. Environ. Sci. Technol. 45 (1), 235–240. https://doi.org/10.1021/es1019146.

Xu, Z.X., Dou, W.W., Chen, S.G., et al., 2022. Limiting nitrate triggered increased EPS film but decreased biocorrosion of copper induced by *Pseudomonas aeruginosa*. Bioelectrochemistry 143, 107990. https://doi.org/10.1016/j.bioelechem.2021.107990.

Xu, D.K., Gu, T.Y., Lovley, D.R., 2023. Microbially mediated metal corrosion. Nat. Rev. Microbiol. 21, 705–718. https://doi.org/10.1038/s41579-023-00920-3.

Yang, Y., Zhou, E.Z., Li, L.K., et al., 2025. The role of phenazines in marine *Pseudomonas aeruginosa* microbiologically influenced corrosion against 316L stainless steel. Corros. Sci. 242, 112587. https://doi.org/10.1016/j.corsci.2024.112587.

Young, C.C., Rekha, P.D., Lai, W.A., et al., 2006. Encapsulation of plant growth-promoting bacteria in alginate beads enriched with humic acid. Biotechnol. Bioeng. 95 (1), 76–83. https://doi.org/10.1002/bit.20957.

Yuan, S.J., Sun, M., Sheng, G.P., et al., 2011. Identification of key constituents and structure of the extracellular polymeric substances excreted by *Bacillus megaterium* TF10 for their flocculation capacity. Environ. Sci. Technol. 45 (3), 1152–1157. https://doi.org/10.1021/es1030905.

Yun, U.J., Park, H.D., 2003. Physical properties of an extracellular polysaccharide produced by *bacillus* sp. CP912. Lett. Appl. Microbiol. 36 (5), 282–287. https://doi.org/10.1046/j.1472-765X.2003.01309.x.

Zhang, D., Wu, J.J., 2020. Research progress on the mechanisms of microbiologically influenced corrosion in marine environment. Oceanol. Limnol. Sinica 51 (4), 821–828. https://doi.org/10.11693/hyhz20200300061.

Zhang, J.R., Li, Z., Sun, W.Y., et al., 2025. Extracellular polysaccharides of *Tenacibaculum mesophilum* D-6 play a major role during its corrosion protection for X80 carbon steel in seawater. Corros. Sci. 249, 112811. https://doi.org/10.1016/j.corsci.2025.112811.